Tellus (2001), 53A, 74–93
Printed in UK. All rights reserved

TELLUS
ISSN 0280–6495

Vapor flux associated with return flow over the Gulf of Mexico: a sensitivity study using adjoint modeling

By J. M. LEWIS[1], K. D. RAEDER[2] and R. M. ERRICO[2], [1]*National Severe Storms Laboratory, Norman, OK, 73069, and Desert Research Institute, Reno, NV, 89506-0220;* [2]*National Center for Atmospheric Research, Boulder, Colorado, 80305, USA*

(Manuscript received 23 June 1999; in final form 17 May 2000)

ABSTRACT

The moisture flux associated with a return-flow event in the Gulf of Mexico is studied with the aid of a regional forecast model and its adjoint. The adjoint model allows us to determine the derivatives of some aspect of the model output (a scalar, J) with respect to elements of the control vector (initial and boundary conditions). We choose J to be the northward moisture flux through a vertical cross section in the northwestern corner of the Gulf at the time when the moisture surge in the US is a maximum. The sensitivities (∇J) are used in conjunction with a set of optimal perturbations to estimate the impact of each of the perturbations on the moisture flux. The perturbations are chosen to have the structure of the sensitivities (making them optimal as described in the text), with magnitudes based on the (assumed) uncertainties in the model's initial and boundary conditions. The linear impact estimate is simply the projection of the perturbation onto the sensitivity fields. In complementary fashion, we introduce perturbations into the nonlinear forecast model and decompose the actual impact on J into thermodynamic and dynamic components, in order to better understand the nature of the sensitivity. From this numerical experiment we conclude the following. J is more sensitive to the temperature field than to the other prognostic variables, roughly by a factor of 3 or 4, based on the optimal perturbations used here. The sensitivity to each of the 3-D prognostic variables peaks in the lower atmosphere near 85 kPa. The sensitivity of J to the sea surface temperature (T_s, a fixed boundary condition) increases with forecast length. More than 30 h before the verification time, the impact of an optimal perturbation to T_s is comparable to the impact of an optimal perturbation to the whole 3-D air temperature field. The zones of sensitivity to the T_s are intimately tied to the trajectories of low-level air which terminate at the cross section. The impact of an optimal perturbation to the topography along the Sierra Madre Oriental mountains is comparable to the impact of optimal perturbations in each of the 3-D prognostic variables (except T).

1. Introduction

Generally, the return-flow phenomenon has the following characteristics: cold, dry air tracks over a warmer, more moist region (usually an ocean), and the evolving synoptic circulation causes the modified air to backtrack or return. In our study, we examine return flow over the Gulf of Mexico. In particular, we focus on analysis of the moisture return during the late phase of the phenomenon.

A conceptual model of return flow has emerged from a series of investigations associated with project GUFMEX (Gulf of Mexico Experiment; Lewis et al., 1989). A collection of these contributions can be found in the special issue of *Journal of Applied Meteorology* (Air–Sea Interaction and Airmass Modification over the Gulf of Mexico; *J. Appl. Meteor.*, 1992).

In the conceptual model, the track and intensity

* Corresponding author.
e-mail: raeder@ncar.ucar.edu

of the cold anticyclone controls the low-level trajectories of air — these trajectories range from sweeping gyres that traverse much of the Gulf to smaller tightly wound cycloids confined to the northern Gulf. These tracks, when coupled with the distribution of sea-surface temperature (T_s), can be used to estimate the turbulent flux of moisture and heat into the atmospheric boundary layer — typically a mixed layer where the distributions of heat and moisture are uniform as evidenced by the constancy of vapor mixing ratio (q) and potential temperature (θ). The mixed layer typically grows upward in response to thermals that are generated by the turbulent flux of heat at the ocean-air interface; but this growth is constrained by the subsidence (adiabatic warming) that is associated with the anticyclone.

The Sierra Madre Oriental mountains act as a barrier to the anticyclonic trajectories in the northwestern Gulf. Consequently, there is a confluence of trajectories along the western boundary of the Gulf. The moisture return is initially concentrated in a narrow corridor straddling the coastal plain and the ocean. As the anticyclone continues to move eastward, this band of moisture flux spreads eastward and northward. Occasionally, the surface moisture return is complemented by the transport of vapor in elevated mixed layers (roughly 50 mb thick layers that form at $\sim$2–3 km above sea level) (Merrill, 1992).

Although operational models generally succeed in forecasting the strength and movement of the synoptic pressure pattern, they often fail to predict the strength and timing of moisture return. Inability to faithfully account for the turbulent transfer at the ocean/air interface has contributed to forecast error, but inadequate depiction of the initial state (especially over the ocean) has unquestionably been problematical (Weiss, 1992; Janish and Lyons, 1992).

As a complement to our conceptual understanding of return flow, we will use a deterministic prediction model to follow the evolution of a particular event. To improve our predictive skill for these synoptic events, we strive to identify those components of the *control vector* (initial conditions and boundary conditions) that have most bearing on the generation, dissipation, and transport of water vapor.

Intuitively, one could change an element of the control vector (holding others fixed) and determine the associated change in some particular model output. This output could simply be the value of a prognostic variable at a point in space and time, or as complicated as the accumulated rainfall over a given area and interval of time. For small perturbation sizes, this effectively determines the first derivative of the chosen output with respect to the changed variable. To the degree that the response is linear with respect to perturbations of interest, knowledge of this first derivative is sufficient to obtain a good estimate of the impacts of such perturbations. To find the complete set of first derivatives by this methodology would require as many model integrations as there are elements in the control vector. For even our simplest deterministic weather prediction models, such a procedure is prohibitive from a computational resource viewpoint. Fortunately, such a brute force approach has been obviated by the development of adjoint modeling. The adjoint approach generates the derivatives with the computational expense of approximately two model forecasts. A tutorial on this methodology can be found in Errico (1997), while applications are found in Hall et al. (1982), and Errico and Vukicevic (1992).

Inherent in the use of adjoint models for these derivative calculations is the specification of the function of the model output that represents the meteorological feature of interest. The function J must be differentiable with respect to the model output. Some features are more difficult than others to characterize in terms of model output. For example, the central pressure of a mid-latitude cyclone may be used to characterize its intensity, but the central pressure is an example of a J that would otherwise be desirable, but is non-differentiable because it involves determining a minimum of a field. In contrast, a J chosen as the surface pressure at a fixed location is a differentiable function of the output. That location may be selected as the point where the minimum surface pressure occurs on the reference (or control) forecast, but it will not necessarily remain the location of the minimum pressure in subsequent perturbed forecasts. The result can be an increase in the pressure at the chosen point, while the central pressure decreases. In contrast, if the feature of interest is the total rainfall over a particular region, then there's no ambiguity; a perturbation may increase it or decrease it, but not both. A better choice for characterizing the intensity of the cyclone might be the average pressure (or vorticity) over some domain that includes the low and some buffer around it to allow for changes in its location.

The sensitivity fields will be most truthful and useful if they are derived from a J which faithfully measures a meteorological feature, regardless of perturbations to the variables used to derive it, when such perturbations do not affect the characteristic of the feature which holds the primary importance. We have chosen our aspect to be the average northward flux of vapor through the "window" in the northwestern corner of the Gulf at the forecast terminus time (Fig. 3). The flux is calculated as the total flux of water vapor (kg s^{-1}) ($v \times q$ summed over the grid boxes in the window, and weighted by mass) divided by the "area" of the window (expressed in m kPa). The window is approximately 550 km wide, and 15 kPa high. In addition to choosing a forecast aspect, we must choose the units for the display of ∇J. We have not found this issue to be discussed thoroughly in the literature, so it is treated in Section 8. Briefly, we desire a form of ∇J that is not overly dependent on the grid representation, but rather, is intimately tied to the mass of air in a grid volume. Thus, as long as the phenomenon under investigation is resolved by the model, then the definition of ∇J linked to mass per grid volume will not exhibit large fluctuations or distortions associated with changes in mesh size.

Following a brief description of the deterministic model and its adjoint, we calculate the derivatives of J with respect to elements of the control vector. Based on the structure of the gradient field, we further explore the causes of sensitivity by perturbing the control vector and analyzing the associated forecasts.

2. Forecast model and its adjoint

2.1. Model

The numerical weather prediction models used in this study are the components of version 2 of the Mesoscale Adjoint Modeling System (MAMS2) developed at the National Center for Atmospheric Research (NCAR; Errico and Raeder, 1998). MAMS2 consists of a limited-area, primitive-equation, nonlinear, forecast model (NLM), described in flux form on an Arakawa B-grid (Arakawa and Lamb, 1977) with a Lambert conformal mapping, as well as its associated tangent-linear (TLM) and adjoint model (AM) components. The time scheme is split-explicit following Madala (1981) with an Asselin (1972) filter to control computational modes. The model includes an adiabatic vertical mode initialization scheme (Bourke and McGregor, 1983) applied to the external and first internal modes.

The model's vertical coordinate is the terrain (z_0) following

$$\sigma = \frac{(p - p_t)}{(p_s - p_t)},$$

where p is pressure, p_t is the pressure at the model's top (set to ~ 1 kPa in this study), and p_s is surface pressure. The horizontal wind components, temperature, and mixing ratio are defined on thirteen levels unequally-spaced in terms of σ, with $\sigma = 0.98$, 0.94, 0.90, 0.86 at the lowest four levels (used to define the moisture flux window) and the remaining nine levels at $\sigma = 0.82$, 0.75, 0.65, 0.55, 0.45, 0.35, 0.25, 0.15, 0.05. The vertical finite differencing follows the energy-conserving formulation of the NCAR Community Climate Model (CCM version 2; Hack et al., 1993).

The moisture flux spans more than four vertical levels and is not oscillatory, so we feel that the phenomenon is well resolved. Whether the sensitivity structures are well resolved must be determined by their examination and consideration of the phenomenon. There is nothing in the figures we present, nor in the many other figures we have examined, to lead us to doubt that this resolution is sufficient to capture the dominant features we seek. Higher resolution might yield more "details," but these would still be suspect due to the linearized nature of the adjoint model.

The NLM is started from analyses produced by the European Center for Medium Range Weather Forecasts (ECMWF) and archived at NCAR on a 128×64 global, Gaussian grid and subsequently interpolated to the MAMS2 grid. The horizontal grid for this study covers the entire Gulf of Mexico and most of the US. It has a nominal resolution of 50 km, and extends 67 points meridionally, and 86 points longitudinally. The model's lateral boundary conditions are formulated using a Davies and Turner (1977) relaxation scheme applied within eight grid points from the edge using a relaxation coefficient that exponentially decreases inwards from the grid's edge. The lateral boundary conditions are obtained from fields linearly interpolated in time between subsequent 12-h analyses produced in the same way as the initial conditions. The sea-surface temperature (T_s) is interpolated from a global, 1° resolution horizontal grid of the weekly (averaged) Reynolds data set that is based on COADS data. It is held constant during the model integration, in contrast to the ground temperature (T_g), which is a prognostic variable. At the initial time, T_g is equal to the lowest level air temperature.

The model physics include a stability-independent bulk formulation of the planetary boundary layer (Deardorff, 1972) and a stability-dependent vertical diffusion following CCM version 3 (Kiehl et al., 1996) and is formulated in terms of an implicit temporal scheme. Horizontal diffusion at interior grid points is implemented by using a fourth-order scheme with a time-independent coefficient applied to wind, temperature, and water vapor (mixing ratio). Diffusion is second-order next to the boundaries. The prognostic equation for ground temperature includes radiative effects and is modeled identically to that in the model described by Anthes et al. (1987), which accounts for fractional cloud coverage by utilizing three cloud levels and a piece-wise linear function of relative humidity. The effects of radiation on the free atmosphere are neglected and a dry convective adjustment scheme is not included in this study.

Moist convection is modeled using the Relaxed Arakawa–Schubert (RAS) scheme developed by Moorthi and Suarez (1992), plus a consideration of down drafts (provided by Moorthi and Suarez) and depth-dependent relaxation time scales. Nonconvective precipitation is simply the result of an energy-conserving adjustment back to 100% relative humidity. Excess moisture is precipitated after approximately accounting for the accompanying increases in temperature and saturation vapor pressure due to condensation. Values for the specific heat of air and latent heat of evaporation are treated as T-independent for this calculation. No evaporation of precipitation falling below the level of condensation is considered.

2.2. *Linearization and adjoint*

The TLM and AM linearizations of MAMS2 are exact, including all the physics, except for two approximations. The first approximation involves the reference state about which the linearization is performed. It is archived at 12-min intervals (every six time steps) rather than every time step. This state is then held fixed during the corresponding period in the TLM or AM. This approximation has negligible impact on the TLM solution except where the perturbation size is smaller than the typical change in the reference state between consecutive time steps. Such perturbations are always present, but measures of the accuracy of the model are dominated by the largest perturbations, making the small perturbation inaccuracy irrelevant. The vertical-mode initialization is particularly useful for limiting high-frequency behavior that would otherwise exceed this condition. This approximation greatly reduces data archiving, data exchange, and some computational requirements (Errico et al., 1993). The second approximation is that Jacobians for moist convection are computed using the perturbation method described in Errico and Raeder (1999). The Jacobians of the moist convection at individual (horizontal) locations are set to zero if, after being time averaged, individual components have large values or any of its eigenvalues are significantly larger than 1 (see Errico and Raeder, 1999 for the motivation for this filtering).

We have judged that the TLM is a good approximation to the nonlinear model where this judgment is based on standard statistical measures of comparison, such as the root-mean-square differences between forecasts; additionally, we have compared the structure and magnitude of the perturbation patterns produced by both models and found high correlation. Therefore, the adjoint sensitivities are good approximations to the nonlinear sensitivities.

3. Synoptic event/model validation

3.1. *Synoptic overview*

The return-flow event we will investigate began on 11 February 1988, shortly before 1200 UTC. As shown in Fig. 1a, a cold front separating continental polar air from maritime tropical air has entered the northwest corner of the Gulf. At this time, surface temperatures along the Texas coast are ~ 5°C, with dewpoints ~ 0°C. There is a strong temperature gradient behind the advancing front

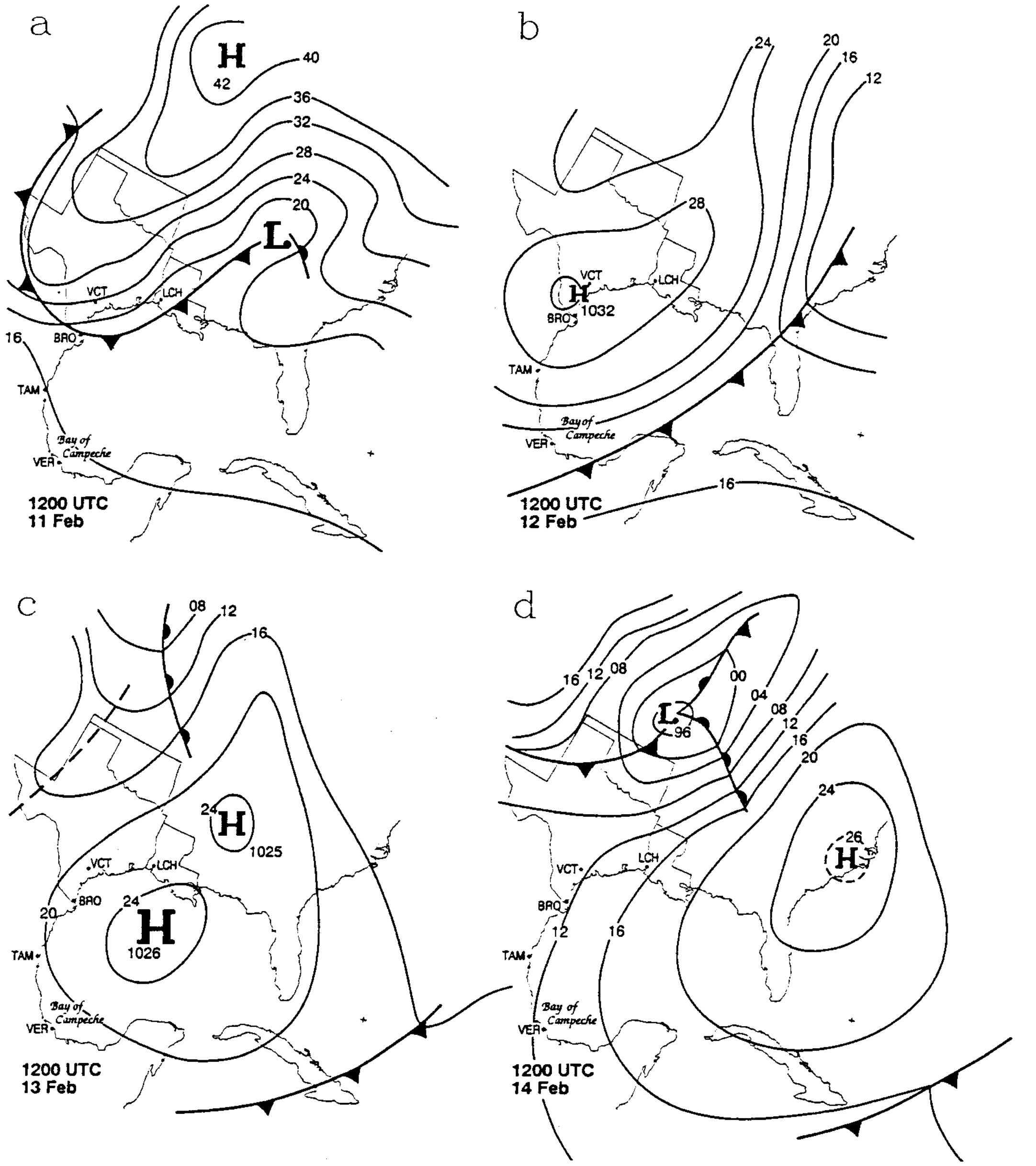

Fig. 1. Surface pressure analyses from the National Hurricane Center, Miami, FL, at 24 h intervals beginning at 1200 UTC, 11 February 1988. Isobars are labeled in mb (millibars) where only the tens and units digits are shown. Fronts and pressure centers are also displayed. The location of various meteorological stations referenced in the text are given, where the following abbreviations apply: LCH (Lake Charles, Louisiana), VCT (Victoria, Texas), BRO (Brownsville, Texas), TAM (Tampico, Mexico), and VER (Veracruz, Mexico).

with (temperatures, dewpoints) $\sim(-15°C, -20°C)$ in central Oklahoma.

The progression of the pressure pattern (and associated fronts) over a three-day period are displayed in Figs. 1a–d. During the first day, the front moves rapidly toward the southeast corner of the Gulf. This occurs in association with movement of the cold anticyclone from the northern Great Plains into the Gulf. Within the next two days, the anticyclone weakens as the center steadily moves from the northwestern Gulf up through the Carolinas. By 1800 UTC on the 12th, the front has swept over the entire Gulf of Mexico and is situated well out into the Caribbean by 1200 UTC, 13 February.

The return flow (southerly flow) commences along the coastal plain southward of Brownsville, Texas (BRO) by 1200 UTC, 13 February. By 0000 UTC, 14 February, the southerly flow spreads eastward and northward while increasing in speed — this is in response to the strong pressure gradient that is generated between the anticyclone and a rapidly developing low pressure system that moves into the central Great Plains by 0000 UTC, 14 February. This depression is located north of Oklahoma as shown in Fig. 1d. The development of low-level jets in these situations has been investigated by Djuric and Ladwig (1983).

The surge of surface moisture occurs along the Texas coast between 1200 UTC, 13 February, and 0000 UTC, 14 February. Brownsville's surface dewpoint jumps from 3C to 13C during this 12 h period. By 1200 UTC, 14 February, the leading edge of this moist air has moved through central Texas. Stratiform clouds are associated with this moisture surge, but there are no reports of precipitation in the south-central states through 1200 UTC, 14 February.

Rawinsonde reports from BRO, VCT (Victoria, Texas) and LCH (Lake Charles, Louisiana) indicate that the marine layer is approximately 10 kPa thick along the Texas coast at 0000 UTC, 14 February. This depth increases to ~ 17 kPa by 1200 UTC, 14 February, as indicated by the thermodynamic profile from Victoria as shown in Fig. 2. The average value of the specific humidity in this marine layer is $\sim 9\ \mathrm{g \cdot kg^{-1}}$ where the value at the top of this layer is lower than that at the bottom due to entrainment of dry air from the overlying subsidence-inversion layer.

In our sensitivity study, we will analyze this return-flow event over the period 0000 UTC, 12 February through 0000 UTC, 14 February. This period covers the 48 h preceding the onset of the moisture surge over the northwestern Gulf and adjoining coastal plain. Since our aspect J will be defined at the latest time, and will be used as a point of reference, we choose to denote 0000 UTC, 14 February, as $t = 0$ in subsequent discussion. Thus, the initial time, 0000 UTC, 12 February, will be denoted by $t = -48$ h.

From an operational viewpoint, the 48 h forecast has special significance, since forecasters at the US Storm Prediction Center (SPC) are required to issue a two-day outlook (for severe weather), and primary guidance for this forecast comes from the operational prediction model.

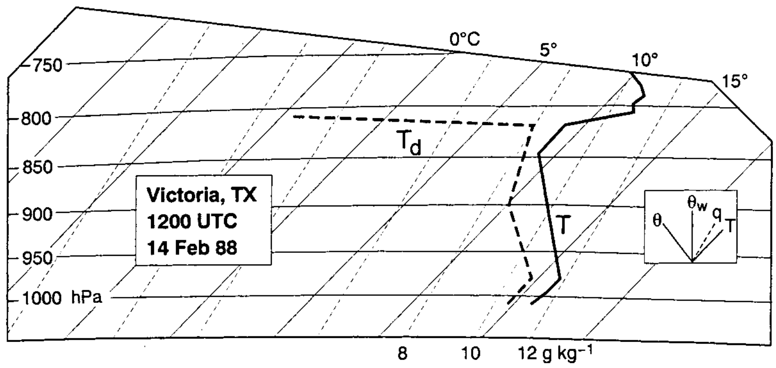

Fig. 2. Temperature and dewpoint temperature from the Victoria, Texas, upper-air station at 1200 UTC, 14 February 1988. The data are plotted on a skew-T/log P thermodynamic chart where temperature (in °C) is labeled along the abscissa and isotherms are the slanted straight lines oriented at 45° angles.

3.2. Forecast model performance

The research model succeeds in capturing the intensity and movement of both the anticyclone and trailing cyclone. Consequently, it faithfully reproduces the strong surface pressure gradient that forms over the southern Great Plains and the northwestern Gulf. Due to the relatively coarse resolution in the lower troposphere, the model is unable to forecast the abrupt changes near the top of the marine layer (near the inversion), but the mean values of the water vapor below the inversion are within ~ 1 g kg^{-1} of the values at the coastal stations.

The northward moisture flux predicted by the model is shown in Figs. 3a,b. Here the plan views

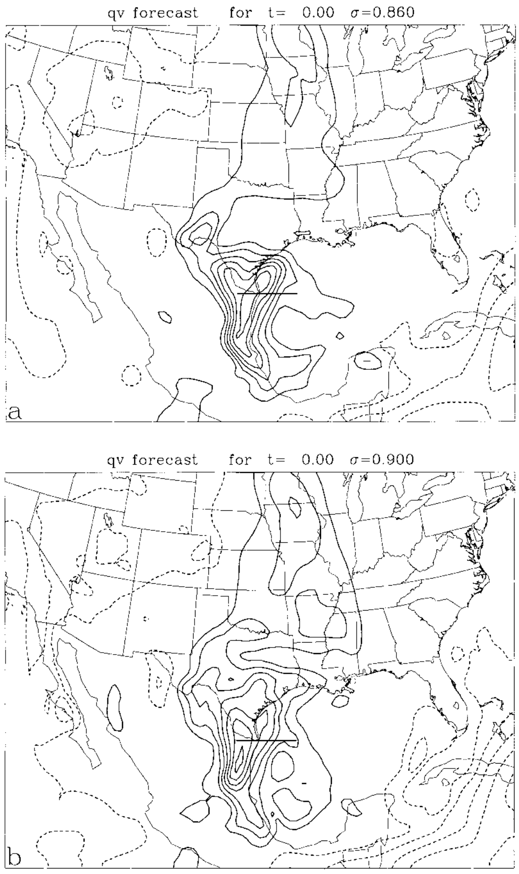

Fig. 3. The 48-h forecast of moisture flux (*qv*) at levels $\sigma = 0.86, 0.90$. The plan view of the cross section is shown as the straight line at the southern tip of Texas. Contour interval is 0.2 m g(s kg)$^{-1}$.

of the flux at $t = 0$, levels $\sigma = 0.90$ and 0.86, indicate a strong band of moisture flux extending along the coastal plain from Veracruz (VER) to Brownsville. The coastal plain along the Gulf's western edge is narrow (~ 50 km wide) and the steep slope of the adjoining Sierra Madre Oriental mountains acts to channel the flow. As the low-level stream approaches Brownsville, it forks northwestward along the Rio Grande Valley and northeastward along the Texas coast. The flux drops off dramatically above $\sigma = 0.86$, which is roughly the top of the marine layer as depicted by the model. This representation of the moisture flux is generally consistent with the analysis, exhibiting more detail and a slightly greater magnitude than the lower-resolution analysis ($\sim 10\%$ greater magnitude).

4. Sensitivity results

4.1. General viewpoint

The conceptual framework for the analysis of sensitivity will be briefly outlined in this section. As mentioned in the introduction, ∇J is a vector whose elements are the derivatives of J (the aspect) with respect to the components of the control vector (initial conditions, boundary conditions, and model parameters). It is a vector whose length is determined by the number of values needed to specify the initial state, augmented by the number of values needed to specify the boundary conditions and the parameters employed in the governing equations. For our model, with four prognostic variables specified at each of the 3D grid points and two prognostic variables at each of the surface points, boundary variables such as sea surface temperature and topography specified at the lower boundary, and model parameters, the total number of elements in ∇J is $\sim 3 \times 10^5$.

Each component of ∇J has the units of J [kg (s m kPa)$^{-1}$] divided by the units of the corresponding element of the control vector, i.e., the units of ∇J are different depending on what part of the control vector is considered. The sign of an element of ∇J gives the sense of the impact on J associated with a positive perturbation. That is, if a particular element of $\nabla J < 0$, then a positive perturbation to that variable will lead to a decrease in J; conversely, a negative perturbation will lead to an increase in J. While the magnitudes of sensitivity to a given field at different locations can be directly compared (if the domain grid is uniform; see Section 8), those of distinct fields cannot because of the differing units. It is necessary to transform them into comparable quantities. The most convenient and relevant quantities are the impacts on the forecast aspect, which result from perturbations to the model fields. Formally, the net change in J is found by finding the projection of ∇J on the perturbed control vector. This net change is given by:

$$J' = \sum_i \left(\frac{\partial J}{\partial x_i}\right) x_i', \tag{1}$$

where $\partial J/\partial x_i$ are the components of ∇J and x_i' are the corresponding perturbations. This assumes that the perturbation size is sufficiently small to insure validity of the tangent linear approximation. In such a case, the model output and J' are linear functions of the perturbed control vector.

Since an impact will depend on both the size and shape of a perturbation, we must be quite specific about our choice. Some care should be taken that the perturbations of various fields are comparable and reasonable. One way to ensure comparable sizes would be to use the same small (but not infinitesimal) fraction of the standard deviation (or other measure of variability) of each field. An example of maintaining reasonableness is the handling of specific humidity, which usually decreases very rapidly with height. Perturbations of 1 g kg^{-1}, which may be reasonable at the surface, are not appropriate at heights where $q < 1$ g kg^{-1}. It is conceivable that a priori knowledge of the analysis system would dictate the introduction of large perturbations in a specified location — for example, over an inland sea where data are relatively scarce compared to the surrounding landmass. Rather than attempting to structure the perturbations based on the suspected distribution of analysis errors over our region, we employ what are known as "optimal perturbations" (see Errico, 1997 for a discussion of the optimality conditions). These perturbations are proportional to the magnitude of the elements of ∇J, viz.,

$$x_i' = a\left(\frac{\partial J}{\partial x_i}\right), \tag{2}$$

where a is a constant for each model level and field. Thus, the spatial structure of the perturbations of each model level and field is identical to the corresponding ∇J pattern. We choose the proportionality constant a as:

$$a = \frac{b}{|\partial J/\partial x_i|_{\max}}, \tag{3}$$

where b is an assumed maximum perturbation. We find $|\partial J/\partial x_i|_{\max}$ for each model variable on a level-by-level basis (2D approach), and assign an associated value of b. Thus, (1) takes the form:

$$J' = \sum_i \frac{b}{(|\partial J/\partial x_i|_{\max})}\left(\frac{\partial J}{\partial x_i}\right)^2, \tag{4}$$

where the summation has an implied partitioning by model variable and level.

Although the definition of J will remain unchanged in our experiments, we find it advantageous to consider different initial conditions. Thus, J is always defined at $t = 0$ (0000 UTC, 14 February), but we will change the control vector. This will allow us to view J' as a function of the forecast duration. We expect to see some temporal continuity in J'; furthermore, the temporal change may suggest a process germane to altering the aspect. However, realizing that multitudinous interactions between model variables contribute to J', it is unrealistic to expect that all processes leading to these changes can be identified.

4.2. *Net impact of model variables on J*

In our first experiment, we attempt to find the relative importance of the various meteorological variables, the sea surface temperature, and topography to J'. Here we will find the integrated effect of each variable by taking the projection of ∇J onto a set of optimal perturbations where the amplitudes b are chosen as follows:

u, v:	1 m s^{-1}	z_0:	100 m
T:	1°C	T_s	1°C
q:	1 g kg^{-1}		

These values are typical of the root mean square analysis errors associated with each variable. Since the impact estimates discussed in this section are linearly determined, impacts for other values of b may be computed by simply multiplying J' by the appropriate factor. Thus, our choice of b is more for convenience rather than being central to the analysis. The arbitrariness in the choice of perturbation size is directly reflected in the resulting impacts. As a result, the significance given to differences in impacts should be considered in the context of that choice. The choice for z_0 is reasonable considering the differences that exist between various terrain height data sets and methods for computing grid box average heights. Although perturbations intended to be consistent with analysis error statistics should account for their spatial dependence, we purposefully neglect this to facilitate comparisons, particularly the impacts due to distinct model levels.

We further assume, for reasons discussed in Section 8, that the perturbations are introduced over equal depths $\Delta\sigma$. This allows us to assess the impact per unit depth. The change to J as a result of introducing these perturbations at $t = -48$ h is shown in Fig. 4. Here we have partitioned the impact by variable and level. The temperature's impact is roughly 3–4 times greater than the other prognostic variables, and the greatest impact is felt near the top level of the cross section ($\sigma = 0.86$).

The total impact of a variable at a given time can be found by integrating the profile over the depth of the model. Thus, the impact is reduced to a scalar. Furthermore, this impact can be calculated for the various forecast intervals: -48 h, -45h, ..., 0 h. These results are displayed in Fig. 5. In addition to making impact calculations for the prognostic variables, the impact of the boundary conditions, T_s and z_0, sea-surface temperature and topography, respectively, are shown in this same figure. Temperature's net impact exceeds that of the other prognostic variables at all times between $t = -48$ h and $t = -3$ h. Only impacts due to q and v, the variables involved in the definition of the aspect, are non-zero at $t = 0$. The influence of T_s increases almost linearly as the forecast interval increases, intimating that the T_s influence on J is cumulative.

As an alternative to the level-by-level basis of defining the perturbations, we can define them three-dimensionally. That is, we use the same philosophy of optimality, but we examine each model variable over 3-D space rather than the sequence of 2-D spaces. This will decrease the mean square perturbation since there will generally be only one point in the domain with the maximum value "b". Since T_s and z_0, are represented by two-dimensional arrays, the impacts will remain unchanged for these fields. The 3-D results are shown in Fig. 6. Now the influence of T_s at the longer forecast periods ($\sim$ greater than 30 h)

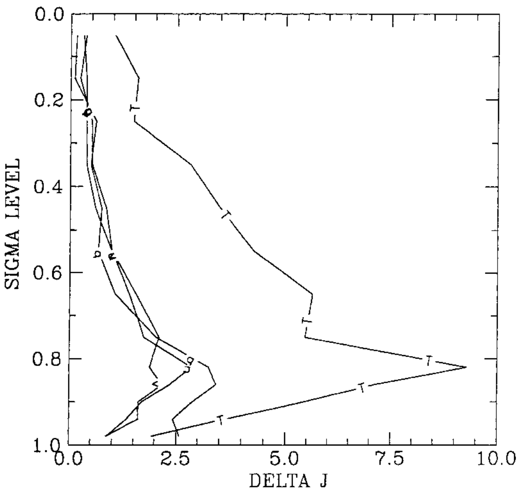

Fig. 4. Vertical distribution of the impact on J due to prognostic-variable perturbations introduced at $t = -48$ h (48 h prior to the time when J is defined).

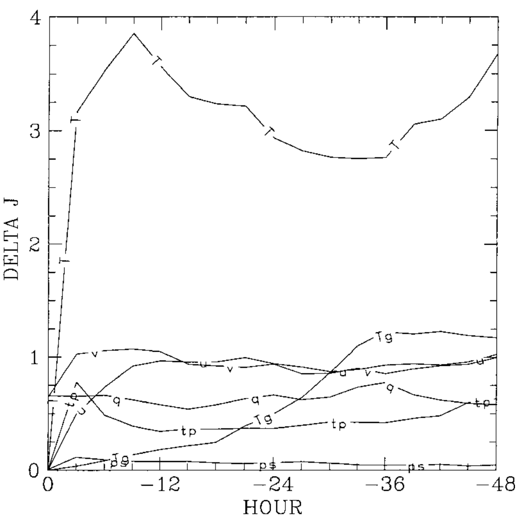

Fig. 5. Net impact on J due to perturbations in the initial state and boundary conditions for a sequence of forecasts of duration 48 h, 45 h, ..., 3 h. The perturbations were "optimal perturbations" on a level-by-level basis. In this diagram, the surface temperature (sea and ground) is denoted by T_g and topography by t_p.

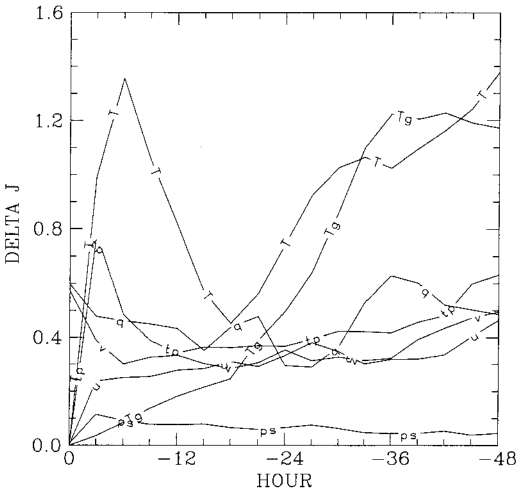

Fig. 6. Net impact on J due to perturbations in the initial state and boundary conditions for a sequence of forecasts of duration 48 h, 45 h, …, 3 h. The perturbations were "optimal perturbations": on a three-dimensional basis.

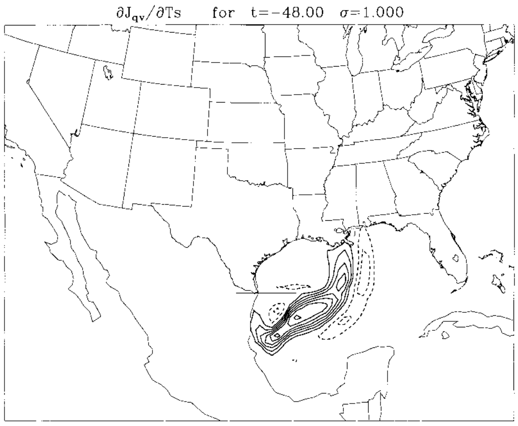

Fig. 7. ∇J for the T_s component of the control vector at $t = -48$ h. The contour interval is 2×10^{-12} kg (s m kPa K)$^{-1}$.

is comparable to that of temperature. The influence of topography shows little change with forecast period, and is comparable in magnitude to the prognostic variables other than temperature.

4.3. *Structure of* ∇J

In this section we examine the spatial and temporal structure of some representative fields. We concentrate on the prognostic variable q and the boundary variable T_s, with brief attention to the topography.

4.3.1. Sea surface temperature. In Fig. 7 we show the derivative of J with respect to T_s at $t = -48$ h. Note that the field is primarily positive with a curved elliptical structure over a limited portion of the Gulf — a region that stretches from the southeastern shoreline of Louisiana to Tampico (TAM) on the coastal plain of Mexico. There is a companion negative area in juxtaposition with the positive area, but its amplitude is roughly a quarter of that in the positive region. The maximum value of the sensitivity is 1.4×10^{-11} kg (s m kPa K)$^{-1}$ and it is located just south of the eastern tip of the cross section.

We know that the marine layer air passing through the cross section at $t = -48$ h has generally followed an anticyclonic trajectory over the Gulf for a 2–3 day period (Lewis and Crisp, 1992). Using the 6-h surface analyses produced at the National Hurricane Center, we have constructed surface trajectories for this case and they are displayed in Fig. 8. The surface air that tracks over the eastern part of the cross section has traversed an area of the Gulf roughly bounded by latitudes (25N, 30N) and longitudes (90W, 95W).

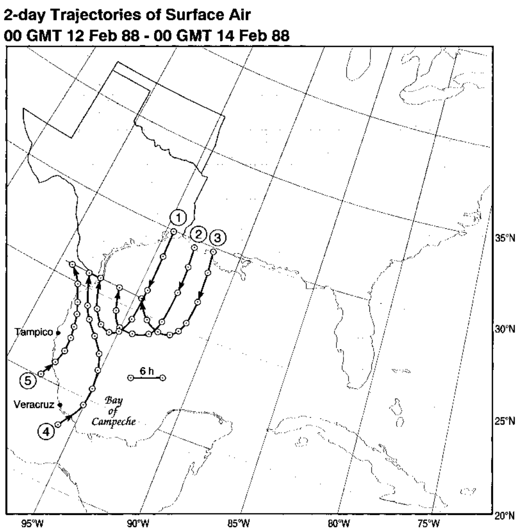

Fig. 8. Trajectories of surface air that terminate at the cross section at $t = 0$, the time when J is defined.

The low-level air coming in through the western segment of the cross section has moved up from the Bay of Campeche along the waters abutting Mexico's coastal plain. Thus, the pattern of sensitivity appears to be controlled, at least in part, by the envelope of 48 h trajectories of surface air that terminate at the cross section at $t = 0$.

One can argue that higher T_s along the path of cold/dry continental air increases the turbulent latent heat transfer from ocean to air — and as a consequence the low-level water vapor increases. This air that is moistened through turbulent transfer is then advected to the cross section along anticyclonic trajectories. This reasoning of course does not account for the presence of the adjoining negative region of sensitivity. There is a dynamical effect too, due to air heating. Cause and effect are difficult to ascertain in this instance.

The sensitivity of the aspect with respect to the T_s boundary condition at $t = -24$ h is displayed in Fig. 9. Positive values still dominate, but the zone of maximum sensitivity is restricted to the area just south and east of the section. Referring back to Fig. 8, we see that the surface air trajectories between $t = 0$ and $t = -24$ h traverse that region of the Gulf just south of the cross section. As the forecast interval decreases, the sensitivity pattern approaches the section from the south.

In light of these patterns of sensitivity associated with T_s, we speculate on the impact of T_s analysis errors on J. We know that the ocean surface temperature over the shelf drops by 1–2 K with the passage of cold/dry air in the cool season (November–March) (Lewis et al., 1997). And as is often the case, cloud cover associated with the frontal passage makes it impossible or difficult to obtain reliable T_s measurements from weather satellites. The instruments aboard the operational satellites rely on infrared radiance measurements and cloud cover contaminates the estimates of T_s. Thus, it is not unusual to have T_s analyses over the Gulf that are based on old data — from several days to a week. This, of course, leads to analysis errors, and if the location of these errors coincide with the zones of sensitivity for a particular return-flow case, then a significant impact on the forecasted moisture flux is likely.

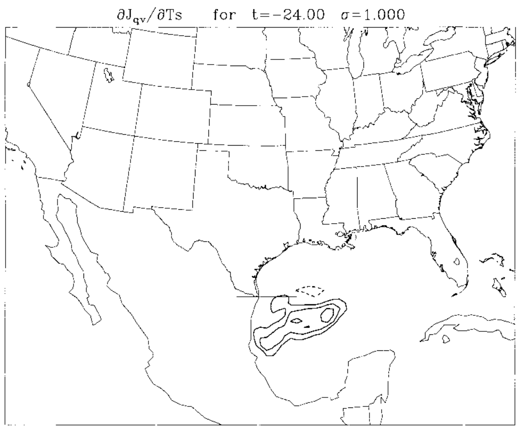

Fig. 9. ∇J for the T_s component of the control vector at $t = -24$ h. The contour interval is 2×10^{-12} kg (s m kPa K)$^{-1}$.

4.3.2. Moisture field. The sensitivity with respect to q at two levels within the cross section (at $t = -48$ h) is shown in Fig. 10. The patterns at both levels exhibit adjoining positive/negative zones, and the spatial scale of the patterns is comparable to that found in the SST sensitivity field. The patterns of sensitivity for these two levels exhibit a marked correlation, i.e., with slight lateral shifts, the positive and negative areas overlie one another.

The zone of maximum sensitivity runs through the state of Louisiana out into the area of shelf water along the Louisiana–Texas coast. Lake Charles, Louisiana, near the Texas–Louisiana border, is located along the western edge of the area of positive sensitivity at $\sigma = 0.86$; at $\sigma = 0.98$, an area of slightly negative sensitivity overlies the LCH location. The LCH thermodynamic sounding at $t = -48$ h (0000 UTC, 12 February) is shown in Fig. 11. There is a shallow mixed layer near the surface (~ 8 kPa thick), overlain by pronounced subsidence inversion. A thin layer of stratus (~ 2.5 kPa thick) is atop the mixed layer. Thus, the $\sigma = 0.98$ level is within the mixed layer and the $\sigma = 0.86$ level is within the dry subsidence layer.

At the location of LCH, a positive perturbation in q at $\sigma = 0.86$ and a negative perturbation at $\sigma = 0.98$ separately lead to an increase in the aspect. Thus, a drier mixed layer and a more-moist subsidence layer would act to increase the moisture flux through the cross-section near Brownsville 48 h later. We will discuss this further in the next section dealing with perturbation forecasts.

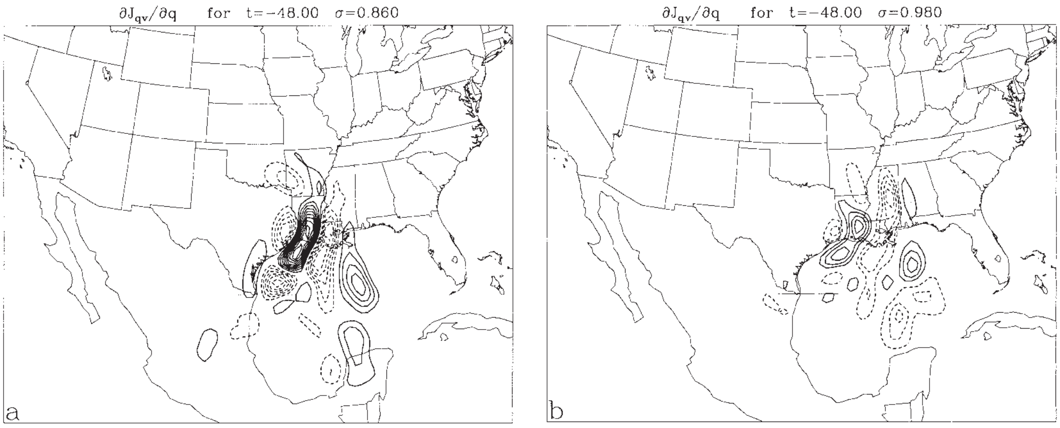

Fig. 10. for the q component at, $\sigma = 0.86, 0.98$, $t = -48$ h. The contour interval is 4×10^{-9} kg (s m kPa g)$^{-1}$.

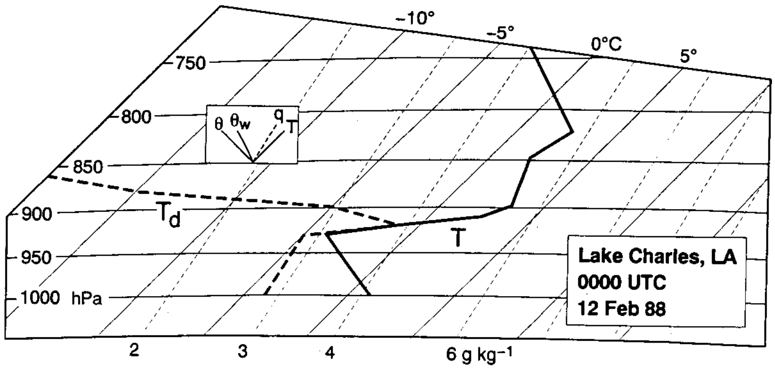

Fig. 11. Themodynamic sounding at Lake Charles, Louisiana, at 0000 UTC, 12 February 1988 (see Fig. 2 caption for chart description).

4.3.3. Topography. Finally, in this section on sensitivity structure, we discuss that component of ∇J related to the topography (a boundary condition). The sensitivities at $t = -48$ h are shown in Fig. 12. There is little difference in the overall pattern between this time and $t = -24$ h, again indicating that the influence of the topography does not exhibit a cumulative effect as does T_s. If positive perturbations to the topography are introduced west of the cross section and southward along the coastal plain of the Sierra Madre Oriental, and up into the high plain west of Veracruz, then the aspect will increase. As shown in Fig. 6, the net effect of introducing perturbations into the topography is comparable to those associated with perturbed initial states of the wind and moisture if we consider perturbation sizes of 100 m comparable to 1 m s^{-1} and 1 g kg^{-1}, respectively. The sensitivities over the Gulf have been set to 0 in these figures, since no meaningful changes to the sea level are possible, although the values are actually larger there than over land.

5. Perturbation analysis

As stated earlier, the linearized estimate of change in the aspect can be found by projecting the perturbation vector onto the sensitivity vector (∇J). A complementary way to calculate the change in aspect with respect to the elements of the control vector is to perturb the control vector and follow the evolution of the nonlinear forecast. This reveals some nonlinear components of the

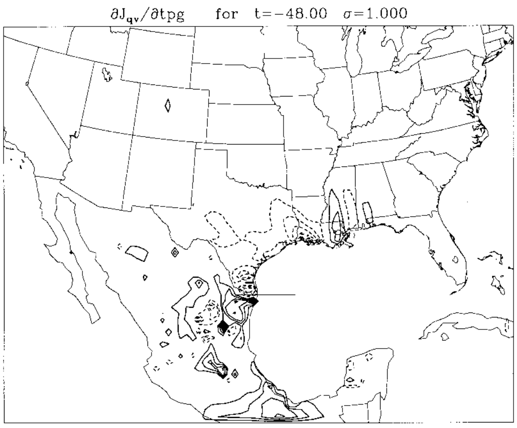

Fig. 12. ∇J for the topographic component of the control vector at $t = -48$ h. The contour interval is 1×10^{-14} kg (s m kPa m)$^{-1}$.

sensitivity, which will depend on the perturbation size. We use the same perturbation sizes discussed in Section 4 to facilitate comparison with the linearized ∇J.

In the following discussion, we use the notation $\overline{(\ldots)}$ to denote the control state which is subtracted from the perturbed state to yield the perturbation $(\ldots)'$.

5.1. *Perturbed sea surface temperature*

In the elongated zone of positive sensitivity to T_s at $t = -48$ h (Fig. 7), we introduce a constant perturbation of 1°C. This area is outlined in the upper-left panel of Fig. 13. The resultant perturbed fields v' and q' at $t = 0$, $\sigma = 0.90$, are shown in the upper-right and lower-left panels of this same figure, respectively. Examination of the fields at the location of the cross section shows that q' is positive, whereas v' is dominantly positive with a weak zone of negative values in mid-cross section. The $(qv)'$ field at this same level is shown in the lower-right panel and it is seen to be positive at the cross section — strongest along the eastern edge, slightly weaker at the western edge, and nearly zero at mid-point.

Partitioning the change of J into a "thermodynamic" component $(q'\bar{v})$, and a "dynamic" component $(\bar{q}v')$, we find that the thermodynamic component is dominant by a factor of ~ 5. The total change in aspect is 1.04 kg (s m kPa)$^{-1}$, and the component changes are 0.94 and 0.17. The residual of -0.06 is due to the second order term $(q'v')$. These results have been displayed along the top row of Table 1.

5.2. *Perturbed moisture*

Optimal perturbations with a maximum magnitude of 1 g kg^{-1} are introduced into the q-field at $t = -48$ h and at the 4 levels of the cross section: $\sigma = 0.98$, 0.94, 0.90, and 0.86. The forecast of q at 2 levels (0.98 and 0.86) and 2 times, $t = -24$ h and $t = 0$, is displayed in Fig. 14. To see the location and structure of the initial perturbations (at $t = -48$ h), refer back to Fig. 10.

There is a definite temporal continuity to the q' pattern at the upper level ($\sigma = 0.86$). The pattern moves from the Louisiana area to mid-Gulf between $t = -48$ and $t = -24$ h, and then the pattern swings northwestward toward the cross section between $t = -24$ h and $t = 0$. At the lower-level ($\sigma = 0.98$), however, pattern continuity is less evident. At the upper level, there is a tendency toward conservation of the perturbed moisture, while there are obvious sources and sinks of moisture at the lower level. These differences in the distributions of moisture lead us to believe that advective transport dominates at the upper level while the changes associated with turbulent transfer are in control at the lower level.

The increase $(qv)'$ in the aspect at $\sigma = 0.86$ due to the perturbation is shown in Fig. 15. We note that an increase is exhibited over the entire width of the section. This pattern is highly correlated with the q'-pattern at $\sigma = 0.86$, $t = 0$, discussed above. Most of the change to the aspect is due to the "thermodynamic" influence (see tabular summary below).

5.3. *Topographic perturbation*

For this experiment, we perturb the topographic field at those locations where the absolute value of sensitivity is greater than 10% of the maximum value. (This strategy eliminates perturbations in the areas of small sensitivity that tend to be noisy. We also screened out large sensitivities which appeared over the ocean because significant height perturbations are not realistic there, and some which appeared on the domain edge, since those appear to be non-physical in origin.) In these areas, we introduce a perturbation of 100 m (refer

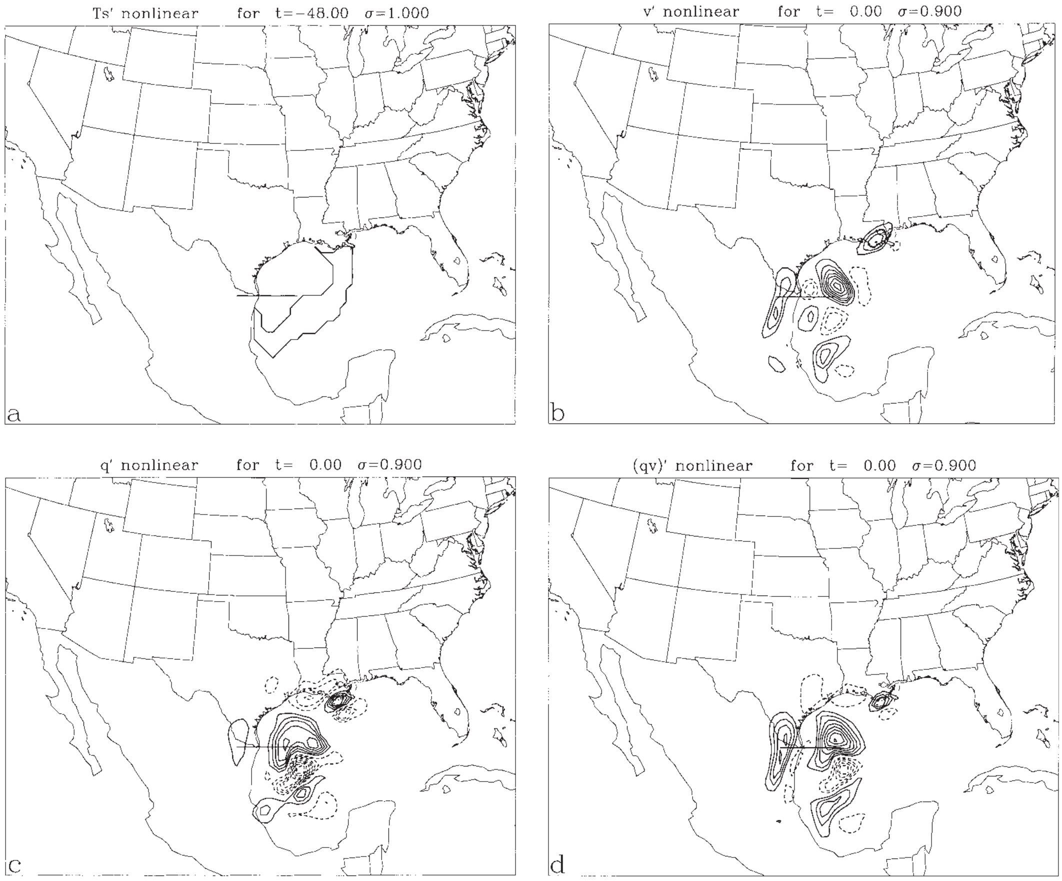

Fig. 13. Results from the experiment that introduced perturbations into the T_s at $t = -48$ h: (a) the zone where a uniform perturbation of 1°C was introduced, interval = 1°C, (b) v' field at $\sigma = 0.90$, $t = 0$, interval = 0.5 m s^{-1}, (c) q' field at $\sigma = 0.90$, $t = 0$, interval = 0.5 m s^{-1}, and (d) $(qv)'$ field at $\sigma = 0.90$, $t = 0$, interval = 0.005 m g (s kg)$^{-1}$.

back to Fig. 12 to view the sensitivity pattern for topography). Over the Sierra Madre, west of Veracruz, the modeled mountains are $\sim$2500 m. The terrain slope is $\sim$2000 m per 200 km (1 : 100) immediately west of Mexico's coastal plain. Since the perturbation magnitude is uniform and the sensitivity is primarily positive, the slope of the perturbed terrain is the same as that of the control run, except at the edges of the perturbation. In Fig. 16 we display $(qv)'$, the difference of moisture flux between the perturbed forecast and the control run at $t = 0$. This forecast at the top level of the cross section, $\sigma = 0.86$, shows a wide swath of positive values that run from the Bay of Campeche up through south-central Texas, primarily over the ocean but including the coastal plain along Mexico's east coast. The pattern at $\sigma = 0.90$ is essentially the same as that at $\sigma = 0.86$, but the pattern at the two lower levels ($\sigma = 0.94, 0.98$) have less impact on J but exhibit a pronounced maximum in $(qv)'$ over the southeastern Gulf and adjoining coastal plain (centered near Veracruz). The net change to the moisture flux due to the topographic perturbation is primarily from the dynamic ($\bar{q}v'$) term (see tabular summary below).

5.4. *Tabular summary*

Table 1 contains a summary of some of the results of the perturbation experiments. The first four columns describe the perturbation: the field perturbed, the pattern used, the level perturbed,

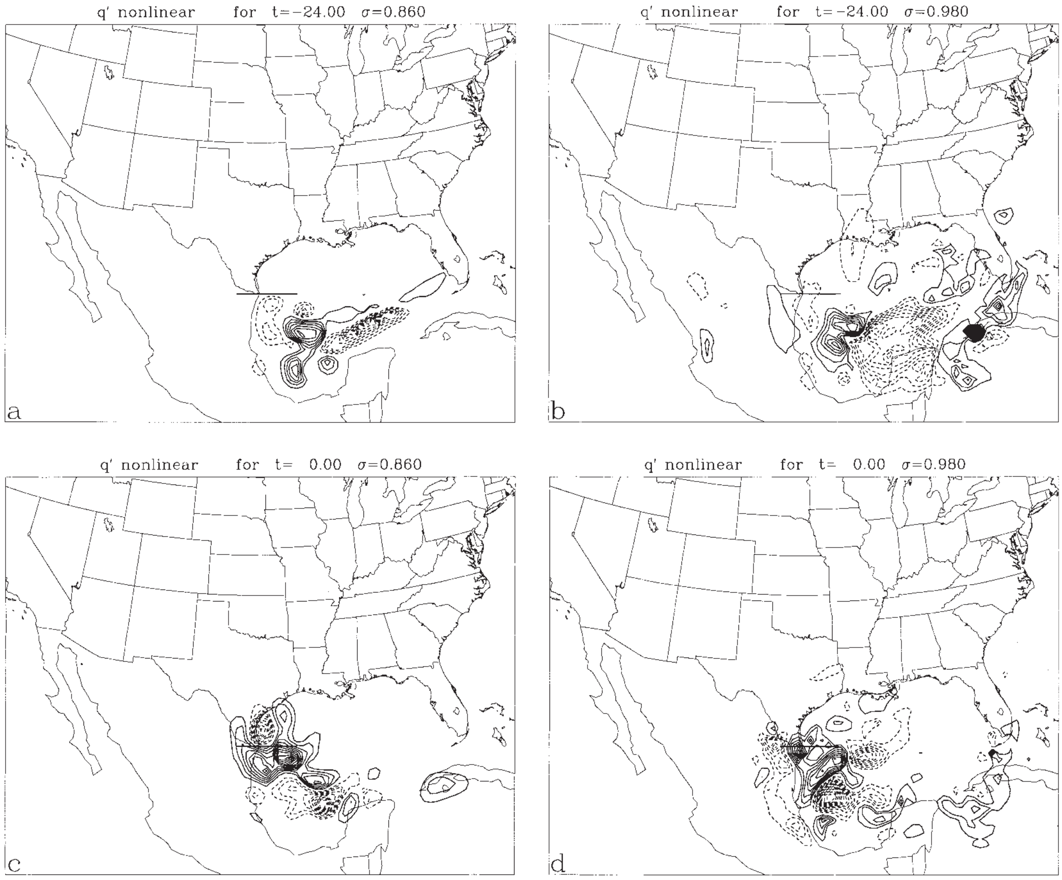

Fig. 14. Results from the experiment that introduced perturbations into the q field at $t = -48$ h. The 4 panels show the q' distribution at two levels ($\sigma = 0.86, 0.98$) and at two times, $t = -24$ h and $t = 0$. Contour interval $= 2 \times 10^{-4}$ g kg^{-1} (a and c) and 2×10^{-5} g kg^{-1} (b and d).

and the size of the perturbation. The 5th column contains the linear estimate of the change to the forecast aspect that each perturbation should produce, based on the projections onto the sensitivities. The 6th column contains the actual J' produced by the perturbation in the nonlinear model. The 5th and 6th columns can be used to judge the utility of the linearization for these particular perturbations; the closer the linear and nonlinear estimates are, the more linear is the regime in which the perturbation is evolving.

All of the perturbation J's are less than 1/4 of the basic state value of moisture flux (7.88 kg (s m kPa)$^{-1}$), implying that these perturbations may be on the border of what's usually thought of as the linear regime. Note the nonlinearity represented by the large linearization error in line 1 versus the small error in line 2. These perturbations used the same perturbation pattern, but with opposite signs; the linear J's are indeed opposites of each other, while the nonlinear J's change size as well as sign. In almost all the perturbations, the linear estimate has a larger magnitude than the nonlinear, implying that some nonlinear processes are acting to limit perturbation growth, rather than augment it. These linearization errors range from a few percent to almost a factor of 2.

The remaining three columns display the partitioning of J' into the linear dynamic ($\bar{q}v'$) and thermodynamic ($q'\bar{v}$) components, and the residual ($q'v'$), which is the nonlinear component. It is interesting to note the disparity between this non-

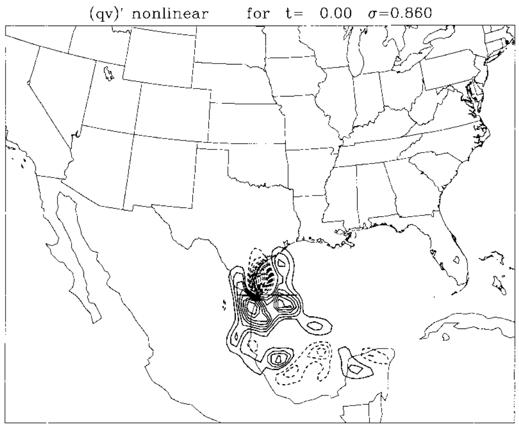

Fig. 15. The $(qv)'$ field at $t = 0$, $\sigma = 0.86$, for the experiment that introduced perturbations into the q field at $t = -48$ h. Contour interval is 0.002 m g (s kg)$^{-1}$.

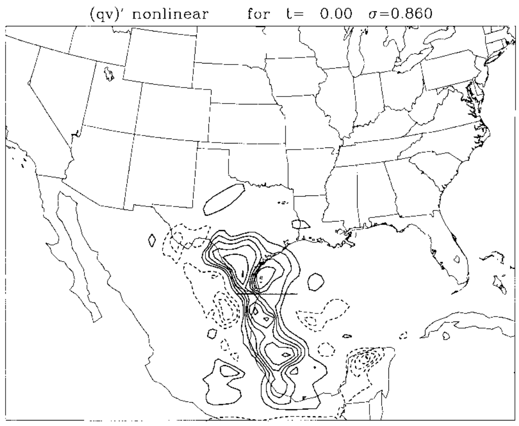

Fig. 16. The $(qv)'$ field at $t = 0$, $\sigma = 0.86$, for the experiment that introduced perturbations into the z_0 field at $t = -48$ h. Contour interval is 0.004 m g (s kg)$^{-1}$.

linear component (column 9), and the difference between the linear and nonlinear J's (columns 5 and 6). They do not match well, implying that nonlinear processes other than the nonlinear definition of J are responsible for the linearization error. Not surprisingly, the thermodynamic component dominates the dynamic component for the T_s and q perturbations, and vice versa for the z_0 perturbation. So the topography primarily affects the amount of air flowing through the cross section, while T_s and q affect the moisture content of that air.

Lines 6 and 7, optimal perturbations of T and q in the bottom four levels of the model, confirm that optimal perturbations of T have more impact than those of q. The importance of the temperature relative to other fields has also been seen in studies of cyclogenesis (Langland et al., 1995). The dynamic component is increased by a factor of 3, while the thermodynamic component increases by only about 20%, but the thermodynamic component is still larger than the dynamic by almost a factor of 2. However, close examination of the basic state and perturbation fields reveals that even this thermodynamic effect is primarily dynamical at root. The T perturbation causes different (moister) air to be advected into the window, rather than moistening the air that was going there anyway. While it is certainly plausible that perturbing the temperature could affect the amount of moisture evaporated from the Gulf if the air is nearly saturated, (a 1 K air temperature increase raises the saturation mixing ratio by roughly 1 g kg^{-1} at these temperatures), in almost every model, the surface moisture flux is determined by the sea-surface temperature (which is held constant in our model) and the moisture content of the lowest level, not by the temperature of the lowest level. This is an illustration of how combining adjoint modeling with impact studies can reveal counter-intuitive causes of intuitive results.

6. Conclusions

Despite our rather clear concept of return flow in the Gulf of Mexico, the operational deterministic prediction of this event remains irascible. In an effort to identify some of the possible problems, we have employed a regional mesoscale model and its adjoint. After establishing the credibility of the model in regard to its portrayal of the return-flow event, we ask the question: how does the influx of moisture through a cross-section in the northwest corner of the Gulf depend on the initial state of the model and associated boundary conditions. We quantitatively answer the question by first defining a forecast aspect J, the average flux of water vapor through the cross section at the time of moisture surge. Then, through backward integration of the adjoint model, we calculate the derivatives of J (∇J) with respect to each element of the control vector. By using an assumed distribution of perturbations in conjunction with ∇J, we determine the impacts of some perturbations on the forecast aspect J.

Our principal results follow.

J exhibits a pronounced positive sensitivity to the T_s (a boundary condition) over an elongated curved region in the northwestern Gulf. This area of sensitivity is linked to the trajectories of the low-level marine layer air that traverse the cross section at $t = 0$, the time when the aspect is measured. Thus, we can isolate those areas of the Gulf where analysis errors will have the most detrimental effect on the vapor flux forecast. Furthermore, the impact of the T_s is cumulative, exhibiting an almost linear dependence on forecast duration.

If we consider the optimal perturbations to the initial and boundary conditions where the maximum perturbation amplitudes are commensurate with nominal analysis errors (see 4b), then the initial temperature field has a net impact on the aspect that exceeds the influence of the other prognostic variables by a factor of ~ 3–4. The effect of changes in the T_s are comparable to those of temperature at $t = -48$ h, but at the shorter forecast periods, temperature becomes relatively more important.

By introducing perturbations into the forecast model, we verify the adjoint model output, i.e., we quantitatively show that placement of a positive/negative perturbation into a zone where ∇J is positive/negative, respectively, leads to an increase in the aspect. Beyond this, we can decompose the influence on the aspect into thermodynamic ($q'\bar{v}$) and dynamic ($\bar{q}v'$) components. The results of this decomposition for various perturbation studies are summarized in Table 1.

For both the thermodynamic and dynamic variable that define the aspect (q and v, respectively), positive and negative zones of sensitivity are of roughly comparable magnitudes. That is, the same sized perturbation at two different points can have opposite effects on the aspect. So if a constant perturbation is applied to the whole region there will be significant cancellation, and the net J' will be much less than the potential J'.

The specification of topography in eastern and southeastern Mexico can influence the aspect. The impact of changes in topography are comparable to those for the initial state variables (except T). This sensitivity to topography is less dependent on the forecast period (for periods longer than 6) than the sensitivity to T_s or T. Its effect is not cumulative, as is the case for T_s. Rather, this influence is more localized (in time) and depends on the evolution of the synoptic low-level wind field in relation to the mountain barrier.

The patterns of the sensitivity fields present information that is not always intuitive, i.e., conceptual understanding of return flow and knowledge of the processes included in the deterministic model are no guarantee that physical interpretation of the sensitivity patterns follow. A good example of this is found in the sensitivity pattern for the T_s. On the one hand, the areal distribution of this pattern follows our intuition — the largest magnitudes are in the northwestern Gulf and are tied to the back trajectories. On the other hand, the $\pm$ pattern is not necessarily expected. In fact, if we were to follow the traditional methodology of testing model sensitivity, we would uniformly increase or decrease the T_s over the shelf water in the northwestern Gulf. This would correspond to the assumption that analysis error due to cloud coverage, for example, would lead to a bias over that region. The uniform perturbation would lead to a reduced effect on the moisture flux due to the cancellation of contributions. The adjoint results precisely tell us where an error in the initial analysis will affect the moisture flux; and furthermore, it tells us the relative impact of a $\pm$ error.

Quantitative results from the adjoint sensitivity analysis have substantiated and confirmed much of what we know about the return flow phenomenon, but the results have also made it clear that there is greater complexity to the phenomenon than we had imagined and, indeed, it will require further diagnostic studies with the model, especially the perturbation forecasts, to uncover the physical basis for some of these sensitivities.

7. Acknowledgments

NCAR is sponsored by the National Science Foundation (NSF). Part of this work was carried out during various visits by the first author to NCAR, with partial financial support through NCAR. Kevin Raeder, NCAR, is partially funded by US Navy Contract N00173-96—MP00152, NASA contract W-19,335, and the US Weather Research Program (USWRP, NSF). The 1-degree,

Table 1. *Summary of impact of various perturbations on J; the basic state value of J is* 7.88 kg (s m kPa)$^{-1}$

Perturbation				Impacts				
field	pattern	level	size	J' (lin)	J' (NL)	$(\bar{q}v')$	$(q'\bar{v})$	$(q'v')$
T_s	>0	surface	1° K	1.86	1.04	0.17	0.94	−0.06
T_s	>0	surface	−1° K	−1.86	−1.71	−0.07	−1.62	−0.01
T_s	<0	surface	1° K	−0.81	−0.52	−0.05	−0.47	−0.01
z_0	>0	surface	100 m	1.10	0.84	0.65	0.22	−0.03
q	<0	1–13	1 g/kg	−0.58	−0.60	−0.11	−0.47	−0.01
q	opt	10–13	1 g/kg	0.37	0.24	0.05	0.19	0.00
T	opt	10–13	max 1 K	0.605	0.456	0.16	0.306	−0.005
T	opt	1–9	max 1 K	1.66	1.08	0.64	0.47	−0.04

Abbreviations: lin: linear; NL: nonlinear; opt: optimal.

weekly sea-surface temperatures were unearthed for us by Steve Worley of the NCAR/SCD/ Data Support Section. We acknowledge Joan O'Bannon, graphic artist at NSSL, for the creation of computer-generated graphics from hand-analyzed weather maps. The comments of anonymous reviewers were very helpful in improving the manuscript.

8. Appendix

The units of ∇J

In deriving the adjoint equations from the TLM equations a norm must be chosen. The norm affects both values and units of the components of the sensitivity fields, which thereby affects their interpretation and use in important ways.

The simplest norm in the context of a numerical model is the Euclidean norm. In a grid point model this may be expressed as

$$I_e = \sum_i \frac{\partial J}{\partial x_i} x_i', \tag{A1}$$

where the summation is over grid points and fields indexed by i, x_i' is the perturbation of the indicated point and field, and $\partial J/\partial x_i$ is the corresponding sensitivity of J with respect to x_i as produced by the adjoint model and I_e is equivalent to a first-order Taylor series approximation to the change of J given x'. Note that no aspects of the model grid (e.g., sizes of each grid volume) are explicitly considered. This norm is perfectly suited for using adjoint model output when considering the effects on J due to explicit perturbations on the model grid as required for data assimilation or some other applications. Most adjoint models, including MAMS2, are formulated using (A1). For some other uses, however, a different norm may be more appropriate, but since the adjoint and TLM are linear models, results for other norms can be determined by simply applying a linear transformation to results generated using the Euclidean norm.

The Euclidean norm may be inappropriate when adjoint-derived sensitivity fields are to be physically interpreted. For such applications, grid-point values are usually intended to be only a representation of a continuously-defined physical field, and it is undesirable for the sensitivity values to incorporate significant distortions due to the grid representation. For example, consider grid resolution. If a sensitivity field is already well resolved, then doubling the resolution in both horizontal directions acts to reduce the magnitude of the sensitivity field by a factor of approximately 1/4. This is because the grid boxes contain only 1/4 as much air, and hence tend to have only 1/4 of the influence on the forecast aspect. Similarly, if the grid resolution varies within the domain, values of sensitivity fields will tend to reflect that variation not only due to physical and dynamical effects, but also because the grid-box sizes vary. Such an effect occurs in this study because the vertical resolution near the surface is $\Delta\sigma = 0.04$ versus $\Delta\sigma = 0.1$ aloft. Sensitivities near the surface are often small due to the strong dissipative process acting there, but the grid spacing itself will further reduce those sensitivities by a factor of 0.4. There are also variations in the horizontal area of each grid box due to the MAMS2 Lambert conformal projection, but these variations are only by a few %.

When sensitivity fields are to be interpreted physically, it is useful to first consider a norm that is defined for continuous fields, i.e., independent of any grid structure. One such norm is

$$I_c = \int \frac{\partial J}{\partial x} x' \, dm, \tag{A2}$$

where dm is a differential unit of air (e.g., a mass or volume) and the integral is over the model domain. The analog of (A2) for grid point fields is

$$I_c = \sum_m \frac{\partial J}{\partial x_{im}} x_i' \Delta m_i. \tag{A3}$$

Notice the difference between this and (A1). They will yield identical results if $\partial J/\partial x_{im}$ is defined as

$$\frac{\partial J}{\partial x_{im}} = \frac{1}{\Delta m_i} \frac{\partial J}{\partial x_i}, \tag{A4}$$

which describes how to transform between sensitivity fields determined with respect to the two norms.

Two obvious choices for Δm_i are volume and mass. Volume has the disadvantage that the density of air decreases exponentially with height, and therefore large volumes of air may have little mass, momentum, heat content, or moisture content. Mass therefore appears a better choice, except that it is a prognostic variable itself (proportional to p_s in a hydrostatic model) and therefore the rescaling or evaluation of the norm would depend on a factor that undergoes perturbations also. Some type of mean value can be used, but other issues remain. Notably, regions with low mass, such as over higher topography will tend to be rescaled by a larger factor, and it may become difficult to distinguish the physical effects of high topography from those simply due to the rescaling.

As a third choice for Δm_i, we have selected

$$\Delta m_i = \Delta A_i \Delta \sigma_i, \tag{A5}$$

where ΔA_i is the horizontal area of a grid box and $\Delta \sigma_i$ is proportional to a fraction of mass per unit area in the grid box. This Δm_i would be proportional to the mass within a grid box if p_s were time and space independent. This choice acts to remove the undesirable effects of varying grid resolution on the sensitivity fields as described above without tampering with any physically-based effects. So, from the output of the adjoint model that is determined for the Euclidean norm we compute

$$\frac{\partial J}{\partial x_{im}} = \frac{\partial J}{\partial x_i} (\Delta A_i \Delta \sigma_i)^{-1}, \tag{A6}$$

when plotting sensitivity fields for subsequent physical interpretation. If x_i corresponds to a surface rather than 3-dimensional field, $\Delta \sigma_i$ is omitted from (A6).

REFERENCES

Anthes, R. A., Hsie, E.-Y. and Kuo, Y.-H. 1987. *Description of the Penn State/NCAR Mesoscale model version 4 (MM4)*. NCAR Technical Note, NCAR/TN-282+STR, 66 pp. (Available from the National Center for Atmospheric Research, PO Box 3000, Boulder, CO 80307, USA).

Arakawa, A. and Lamb, V. R. 1977. Computational design of the basic dynamical processes of the UCLA general circulation model. *Methods in Computational Physics* **17** (Julius Chang, ed.). Academic Press, pp. 174–264.

Asselin, R. 1972. Frequency filter for time integration. *Mon. Wea. Rev.* **100**, 487–490.

Bourke, W. and McGregor, J. L. 1983. A nonlinear vertical mode initialization scheme for a limited area prediction model. *Mon. Wea. Rev.* **111**, 2285–2297.

Davies, H. C. and Turner, R. E. 1977. Updating prediction models by dynamical relaxation: An examination of the technique. *Quart. J. Roy. Meteor. Soc.* **103**, 225–245.

Deardorff, J. W. 1972. Parameterization of the planetary boundary layer for use in general circulation models. *Mon. Wea. Rev.* **100**, 93–106.

Djuric, D. and Ladwig, D. 1983. Southerly low-level jets in the winter cyclones of the Southwestern Great Plains. *Mon. Wea. Rev.* **111**, 2275–2281.

Errico, R. and Raeder, K. 1999. An examination of the accuracy of the linearization of a mesoscale model with moist physics. *Quart. J. Roy. Meteor. Soc.* **125**, 169–195.

Errico, R. 1997. What is an adjoint model? *Bull. Amer. Meteor. Soc.* **78**, 2577–2591.

Errico, R., Vukicevic, T. and Raeder, K. 1993: Examination of the accuracy of a tangent linear model. *Tellus* **45A**, 462–497.

Errico, R. and Vukicevic, T. 1992: Sensitivity analysis using an adjoint of the PSU-NCAR mesoscale model. *Mon. Wea. Rev.* **120**, 1644–1660.

Hack, J. J., Boville, B. A. Briegleb, B. A., Kiehl, J. T., Rasch, P. J. and Williamson, D. L. 1993. *Description of the NCAR Community Climate Model (CCM2)*. NCAR Technical Note, NCAR/TN-382+STR, 160 pp. (Available from NCAR, PO Box 3000, Boulder, CO 80307–3000, USA).

Hall, M., Cacuci, D. and Schlesinger, M. 1982. Sensitivity analysis of a radiative convective model by the adjoint method. *J. Atmos. Sci.* **39**, 2050–2083.

Janish, P. and Lyons, S. 1992. NGM performance during cold-air outbreaks and periods of return flow over the Gulf of Mexico with emphasis on moisture field evolution. *J. Appl. Meteor.* **31**, 995–1017.

J. Applied Meteorology, 1992. Air–Sea Interaction and Airmass Modification over the Gulf of Mexico (Special Issue). *J. Appl. Meteor.* **31**, 819–1017.

Kiehl, J. T., Hack, J. J., Bonan, G. B., Boville, B. A., Briegleb, B. A., Williamson, D. L. and Rasch, P. J. 1996. *Description of the NCAR Community Climate Model (CCM3)*. NCAR Technical Note, NCAR/TN-420+STR, 160pp. (Available from NCAR, PO Box 3000, Boulder, CO 80307-3000, USA).

Langland, R. H., Elsberry, R. L. and Errico, R. M. 1995. Evaluation of physical processes in an idealized extratropical cyclone using adjoint sensitivity. *Quart. J. Roy. Meteor. Soc.* **121**, 1349–1386.

Lewis, J., Martin, W. and Guinasso, N. 1997. Bowen ratio estimates in return flow over the Gulf of Mexico. *J. of Geophys. Res.* **102**, 10535–10544.

Lewis, J. and Crisp, C. 1992. Return flow in the Gulf of Mexico. Part II: variability in return-flow thermodynamics inferred from trajectories over the Gulf. *J. Appl. Meteor.* **31**, 882–898.

Lewis, J., Hayden, C., Merrill, R. and Schneider, J. 1989: GUFMEX: a study of return flow in the Gulf of Mexico. *Bull. Amer. Meteor. Soc.* **70**, 24–29.

Madala, R. V. 1981. Efficient time integration schemes for atmosphere and ocean models. *Finite-difference techniques for vectorized fluid dynamics calculations*, D. L. Book, Ed., Springer, pp. 56–74.

Merrill, R. 1992. Synoptic analysis of the GUFMEX return-flow event of 10–12 March 1988. *J. Appl. Meteor.* **31**, 849–867.

Moorthi, S. and Suarez, M. J. 1992. Relaxed Arakawa–Schubert: a parameterization of moist convection for general circulation models. *Mon. Wea. Rev.* **120**, 978–1002.

Reynolds, R. W. and Smith, T. S. 1994. Improved global sea surface temperature analyses. *J. Climate* **7**, 929–948.

Weiss, S. 1992. Some aspects of forecasting severe thunderstorms during cool-season return-flow episodes. *J. Appl. Meteor.* **31**, 964–982.